ACS APPLIED MATERIALS & INTERFACES

Research Article

www.acsami.org

Porphyrinic Metal–Organic Framework-Templated Fe–Ni–P/Reduced Graphene Oxide for Efficient Electrocatalytic Oxygen Evolution

Xinzuo Fang, Long Jiao, Rui Zhang, and Hai-Long Jiang*

Hefei National Laboratory for Physical Sciences at the Microscale, CAS Key Laboratory of Soft Matter Chemistry, Collaborative Innovation Center of Suzhou Nano Science and Technology, Department of Chemistry, University of Science and Technology of China, Hefei, Anhui 230026, P. R. China

Supporting Information

ABSTRACT: The sluggish kinetics of oxygen evolution reaction (OER) hampers the H_2 production by H_2O electrolysis, and it is very important for the development of highly efficient and low-priced OER catalysts. Herein, a representative metalloporphyrinic MOF, PCN-600-Ni, integrated with graphene oxide (GO), serves as an ideal precursor and template to afford bimetallic iron–nickel phosphide/reduced graphene oxide composite (denoted as Fe–Ni–P/rGO-*T*; *T* represents pyrolysis temperature) via pyrolysis and subsequent phosphidation process. Thanks to the highly porous structure, the synergetic effect of Fe and Ni elements in bimetallic phosphide, and the good conductivity endowed by rGO, the optimized Fe–Ni–P/rGO-400 exhibits remarkable OER activity in 1 M KOH solution, affording an extremely low overpotential of 240 mV at 10 mA/cm^2, which is far superior to the commercial IrO_2 and among the best in all non-noble metal-based electrocatalysts.

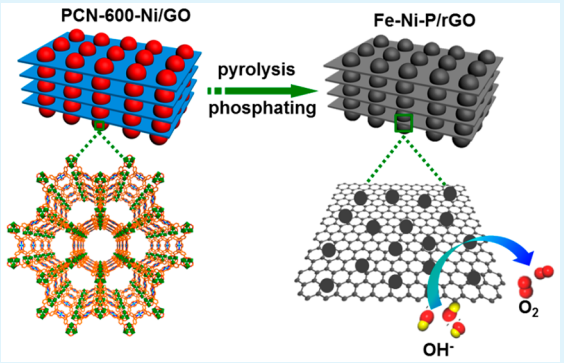

KEYWORDS: *porphyrinic metal–organic framework, transition metal phosphides, electrocatalysts, porous materials, oxygen evolution reaction*

INTRODUCTION

The increased environmental pollution and shortage of fossil fuel have spurred an urgent demand to develop alternative clean energy. Hydrogen (H_2) as the most ideal green energy is attractive and has drawn much attention. Electrocatalytic water splitting, composed of oxygen evolution reaction (OER) and hydrogen evolution reaction (HER), is widely considered to be a promising means to produce H_2 through energy conversion of electricity.[1−9] In principle, the anodic OER process, involving the cleavage of O–H bond and the formation of O=O bond accompanied by the process of four-electron transfer at a high overpotential, is a thermodynamically uphill reaction and determines the rate of the overall water splitting.[10−20] Currently, the commercial electrocatalysts for oxygen evolution reaction are noble metals (Ru, Ir) and their oxides. However, the large-scale application of noble metals in water splitting is hampered due to the high cost and scarcity. Therefore, it is urgently desired to synthesize the noble-metal-substituted OER catalysts with high efficiency and low cost.

Recently, much effort has focused on the synthesis of stable, earth-abundant, transition metal (Fe, Mn, Ni, etc.) based catalysts, such as their nanoparticles, oxides/hydroxides, and layered double hydroxide, etc., as promising substitutions for efficient OER.[21−30] Meanwhile, transition metal phosphides have been recognized to be a new class of efficient electrocatalysts with superior activity, low cost, and good stability.[31−49] To further improve their activity, various strategies have been developed, among which, bimetallic phosphides, being able to manipulate valence and electronic state of the metal elements, have demonstrated to present much better performance than their monometallic phosphide counterparts.[38−43] Apart from tailoring the electronic structure by elemental doping, the exposure of active sites by fabricating porous nanostructure and the enhancement of electronic conductivity by coupling with conductive matrices would further improve the performance of electrocatalysts.[44−49]

With the aforementioned considerations, metal–organic frameworks (MOFs),[50−54] a class of crystalline porous materials assembled by metal ions and versatile organic linkers, might be ideal precursors and/or templates to integrate the above strategies for improving electrocatalytic performance.[55−63] It is able to afford high surface area, variable element species, and homogeneous distribution of different active sites in MOF-derived catalysts by simply regulating the structure/composition of MOFs.[64−70] Porphyrinic MOFs are ideal precursors/templates as they offer alterable metal ions in

Received: May 20, 2017
Accepted: June 27, 2017
Published: June 27, 2017

DOI: 10.1021/acsami.7b07142
ACS Appl. Mater. Interfaces 2017, 9, 23852−23858

both metal clusters and the metal centers in porphyrin linkers toward the formation of highly porous bimetallic phosphides. To further improve the poor electronic conductivity of metal phosphides, the rational integration of them with highly conductive materials, such as graphene oxide (GO), to give hybrid nanocomposites might facilitate to exert their respective merits and realize synergistic effect for enhanced electrochemical activity.

In this work, a representative porphyrinic MOF, PCN-600-Ni,[71] involving Fe_3O clusters as secondary building units (SBUs) and Ni(II) located in the center of porphyrin linkers, was rationally grown onto 2D GO to afford PCN-600-Ni/GO composite. Upon subsequent pyrolysis and phosphidation process, sheetlike Fe−Ni−P/reduced graphene oxide composite (denoted as Fe−Ni−P/rGO-*T*; *T* represents oxidation temperature) can be obtained (Scheme 1). The porous Fe−Ni−P nanostructure inherited from PCN-600-Ni enables the high exposure of active sites as well as the fast process of mass transfer. The coexistence of Fe and Ni elements results in the synergistically enhanced OER activity. Furthermore, the close contact between Fe−Ni−P and rGO leads to a successive conductive network, which is beneficial to the fast electron transfer. As a result, the optimized Fe−Ni−P/rGO-400 exhibits superb catalytic activity for OER with an extremely low overpotential of 240 mV at 10 mA/cm^2 in 1 M KOH solution, and this is far superior to the commercial IrO_2, among the best in all non-noble metal-based electrocatalysts.

Scheme 1. Schematic Illustration Exhibiting the Stepwise Fabrication of Fe−Ni−P/rGO-*T* Composite

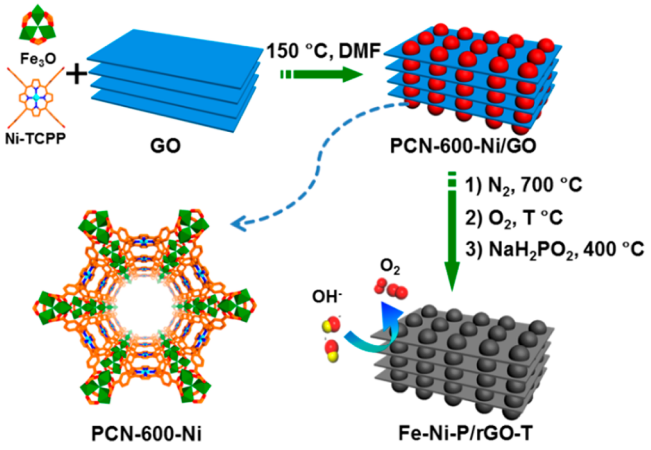

EXPERIMENTAL SECTION

Materials and Instrumentation. The chemical agents were purchased from commercial suppliers without purification unless otherwise mentioned. Methyl *p*-formylbenzoate and pyrrole were obtained from Energy Chemical. $FeCl_2·4H_2O$, $NiCl_2·6H_2O$, $Fe(NO_3)_3·9H_2O$, and $NaOOCCH_3·3H_2O$ were purchased from Sinopharm Chemical Reagent Co., Ltd. Graphene oxide (GO), iridium oxide (IrO_2), and Nafion solution were obtained from Alfa-Aesar. Propionic acid was from Aladdin Industrial Inc.

Deionized water was obtained by reversed osmosis (Cleaned Water Treatment Co., Ltd., Hefei, the specific resistance of 18.25 MΩ·cm). The powder X-ray diffraction (XRD) patterns were carried out at the Japan Rigaku DMax-γA rotation anode X-ray diffractometer. The scanning electron microscopy (SEM) images were obtained from the field emission scanning electron microanalyzer (Zeiss Supra 40 scanning electron microscope). The transmission electron microscopy (TEM) images and the high-resolution TEM (HRTEM) images were obtained through the field emission transmission electron microscope (JEOL-2100F). The X-ray photoelectron spectroscopy (XPS) analysis was carried out at the ESCALAB 250Xi high-performance electron spectrometer. The N_2 sorption measurement was conducted through the automatic volumetric adsorption equipment (Micrometrics ASAP 2020) at 77 K. Before the nitrogen adsorption/desorption measurements were performed, all samples were dried at 150 °C under vacuum for 24 h.

Synthesis of Samples. *Synthesis of Ni-TCPP.* The Ni-TCPP ligand was obtained according to the reported procedure with minor modifications.[71] Typically, methyl *p*-formylbenzoate (6.9 g) and pyrrole (3.0 g) were added into a three-necked flask and dissolved with 100 mL of propionic acid. The solution was refluxed at 160 °C for 12 h and then cooled down to room temperature. Through filtration, rinsed in ethanol, ethyl acetate, and tetrahydrofuran, the precipitate was gathered and finally dried under vacuum at 60 °C for 12 h.

The obtained precipitate (0.854 g) and $NiCl_2·6H_2O$ (3.1 g) were dissolved in 100 mL of dimethylformamide, and the solution was refluxed at 140 °C for 6 h. When the mixture was cooled, the solution was precipitated after another 150 mL of deionized water was added. After being washed with cold deionized water, the solid was redissolved with $CHCl_3$, followed by washing with diluted HCl solution and deionized water. The quantitative crimson solids were obtained through evaporating the organic layer with rotatory evaporator.

The obtained crimson crystals (0.75 g) were dissolved in tetrahydrofuran (25 mL) and methanol (25 mL) mixed solvent, to which 25 mL aqueous solution of KOH (2.63 g) was added. This system was stirred for 12 h and cooled down to room temperature. Deionized water was added to the mixture until the uniform solution was formed, and then the solution was treated with dilute HCl solution. The product was gathered by filtration, cleaned with deionized water, and desiccated at 60 °C for 12 h. Then the Ni-TCPP was obtained.

The Fe-TCPP was obtained through a similar procedure by replacing $NiCl_2·6H_2O$ with $FeCl_2·4H_2O$.

Synthesis of $[Fe_3O(OOCCH_3)_6OH]·2H_2O$. The $[Fe_3O(OOCCH_3)_6OH]·2H_2O$ SBU was synthesized based on a reported procedure with some modifications.[71] Typically, $Fe(NO_3)_3·9H_2O$ (8 g) and $Na(OOCCH_3)·3H_2O$ (11 g) were added to 9 mL of deionized water, which were stirred without heating until the precipitation occurred. The precipitation was filtered and washed by cold deionized water and then desiccated in an oven for 12 h at 100 °C.

Synthesis of PCN-600-Ni. The PCN-600-Ni was fabricated in accordance with the previous works with slight modifications.[71] Typically, $[Fe_3O(OOCCH_3)_6OH]·2H_2O$ (80 mg) was dissolved in 5 mL of dimethylformamide in a 20 mL Pyrex vial by ultrasonication, to which 11 mL of dimethylformamide containing 80 mg of Ni-TCPP and 2.4 mL of trifluoroacetic acid was added. After being kept in an oven for 12 h at 150 °C, the purple crystals were obtained in the Pyrex vial. Through careful washing and supercritical CO_2 drying process, PCN-600-Ni was obtained.

Synthesis of PCN-600-Fe. The PCN-600-Fe was obtained in a similar procedure. Typically $[Fe_3O(OOCCH_3)_6OH]·2H_2O$ (80 mg) was dispersed with 5 mL of dimethylformamide at a 20 mL Pyrex vial by ultrasonication, to which 11 mL of dimethylformamide containing 80 mg of Fe-TCPP and 2.4 mL of trifluoroacetic acid was added. After being kept in oven for 12 h at 150 °C, the purple crystals were obtained in the Pyrex vial. Through careful washing and supercritical CO_2 drying process, the PCN-600-Fe was obtained.

Synthesis of PCN-600-Ni/GO. Typically, 80 mg of $[Fe_3O(OOCCH_3)_6OH]·2H_2O$ and 5 mg of GO were mixed in 5 mL of dimethylformamide at the 20 mL Pyrex vial by ultrasonication, to which 11 mL of dimethylformamide containing 80 mg of Ni-TCPP and 2.4 mL of trifluoroacetic acid was added. After being kept in oven for 12 h at 150 °C, the purple crystals were obtained in the Pyrex vial. Followed by careful washing and supercritical CO_2 drying process, the PCN-600-Ni/GO was obtained.

DOI: 10.1021/acsami.7b07142
ACS Appl. Mater. Interfaces 2017, 9, 23852−23858

Synthesis of Fe−Ni−P/rGO-400. The PCN-600-Ni/GO was heated to 700 °C within 140 min, holding at 700 °C for 10 min in the N_2 protection. Then the material was transferred to the electric muffle furnace and heated at 400 °C for 2 h in air to obtain the Fe−Ni−O/rGO-400. Contrastively, Fe−Ni−O/rGO-350 and Fe−Ni−O/rGO-450 can also be obtained through a similar method by changing the temperature of oxidation process to 350 and 450 °C, separately. Then 10 mg of Fe−Ni−O/rGO-400 and 100 mg of NaH_2PO_2 were placed at the separate positions of a ceramic crucible. The ceramic crucible underwent heat treatment at 400 °C for 2 h. Next, the powder was soaked with dilute HCl solution and washed with deionized water and ethanol. After drying, the Fe−Ni−P/rGO-400 was obtained. Fe−Ni−P/rGO-350 and Fe−Ni−P/rGO-450 were synthesized via the same phosphidation treatment starting from Fe−Ni−O/rGO-350 and Fe−Ni−O/rGO-450, separately.

Synthesis of FeP-400 and Fe−Ni−P. The FeP-400 and Fe−Ni−P-400 were produced from PCN-600-Fe and PCN-600-Ni with the similar process described above.

Synthesis of Fe−Ni−P-GO-Mix. The Fe−Ni−P-GO-mix was produced from the physical mixture of PCN-600-Ni and GO with the similar process for the fabrication of Fe−Ni−P/rGO-400 sample.

Electrochemical Measurement. The electrochemical measurements for all samples were tested with a CHI760E electrochemical analyzer equipped with a rotating disk electrode at 1600 rpm. Typically, a three-electrode setup, with Ag/AgCl serving as the reference electrode and platinum serving as the counter electrode, was used for all electrochemical measurements. The electrochemical measurements were performed in O_2-saturated 1 M KOH solution. 2 mg of catalyst was dispersed with 1 mL of ethanol containing 0.01 mL of 5 wt % Nafion and sonicated for 0.5 h; then the obtained homogeneous ink was dropped onto the glass carbon electrode (loading amount: ~0.3 mg/cm^2). The catalyst was pretreated via cyclic voltammetry (CV) scans at 100 mV/s before the electrochemical OER performance was tested. The linear sweep voltammetry (LSV) test was performed at 5 mV/s. The data were presented without *iR* compensation.

RESULTS AND DISCUSSION

The PCN-600-Ni, formulated as $Fe_3O(Ni\text{-}TCPP)_{1.5}(OH)$ based on Fe_3O clusters and nickel(II) tetracarboxylate porphyrin (Ni-TCPP) linkers, features a well-defined 3D porous structure with 1D channels as large as 3.1 nm (Scheme 2). The GO was introduced to the growth solution of PCN-600-Ni serving as template for the effective synthesis of PCN-600-Ni/GO composite with template-directed sheetlike morphology, possessing a high Brunauer−Emmett−Teller (BET) surface area reaching to 1250 m^2/g (Figures S1−S3). Upon pyrolysis at 700 °C in a N_2 atmosphere followed by oxidation treatment with different temperatures, the obtained Fe−Ni−O/rGO-*T* (*T* represents the oxidation temperature) remains the sheetlike structure (Figures S4 and S5), and its BET surface area reaches to 59 m^2/g, owing to high porosity of the parent PCN-600-Ni (Figure S6). Further phosphidation process gives Fe−Ni−P/rGO-*T* (*T* = 350, 400, and 450) composites with crystalline structure, as approved by the distinct powder X-ray diffraction (XRD) profiles (Figure S7). The resultant Fe−Ni−P/rGO-400, as a representative, clearly shows the thickness about 150 nm with sheetlike morphology (Figure 1a). The hierarchically porous character, especially mesopores in Fe−Ni−P/rGO-400 (Figure S8), which should be partially inherited by the porous character of MOF precursor, accords well with the transmission electron microscopy (TEM) (Figure 1b). The high-resolution transmission electron microscopy (HRTEM) images reveal obvious lattice distance of 0.19 and 0.28 nm, which are correlative with the (211) plane of FeP and (020) plane of NiP_2, respectively, further confirming the successful fabrication of crystalline FeP and NiP_2 species, in consistence with the powder XRD results (Figure 1c,d and Figure S7).

Scheme 2. 3D Network of PCN-600-Ni, Constructed by D_{4h} Porphyrin Linkers and D_{3h} Fe_3O SBUs

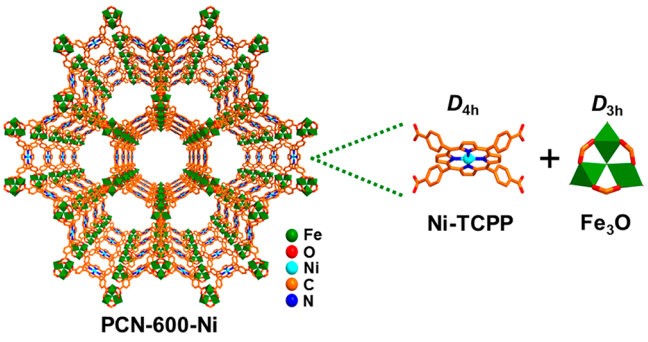

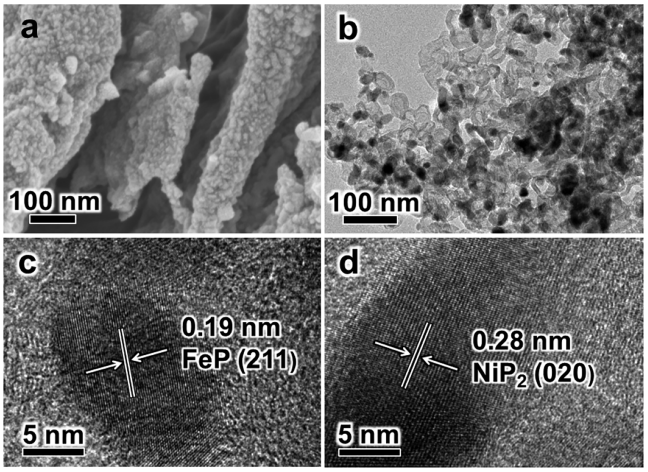

Figure 1. (a) Scanning electron microscopy (SEM) and (b) transmission electron microscopy (TEM) images of Fe−Ni−P/rGO-400. High-resolution TEM images involving (c) FeP and (d) NiP_2 species in Fe−Ni−P/rGO-400.

To further illustrate the chemical composition and related valences in Fe−Ni−P/rGO-400, X-ray photoelectron spectroscopy (XPS) analysis has been performed. As exhibited in Figure 2a, the XPS survey spectrum clearly indicates the presence of C, N, P, Fe, and Ni. More precisely, the high-resolution N 1s spectrum can be fitted into three subpeaks, in accordance with the graphitic-N, pyrrolic-N, and pyridinic-N (Figure S9). It has been reported that the carbon atoms neighboring the nitrogen atom are positively charged due to the higher electronegativity of nitrogen, leading to the much easier adsorption of OH^-, which is beneficial to the OER.[72−74] The high-resolution P 2p spectrum might be fitted into three subpeaks at 129.4, 130.5, and 133.4 eV, corresponding to P $2p_{3/2}$, P $2p_{1/2}$, and oxidized phosphorus species formed on the surface of Fe−Ni−P/rGO-400. The binding energy of P 2p at 129.4 eV shifts negatively, compared with the binding energy of elemental P at 130.2 eV. This indicates that the P element is partially negatively charged because the electron is transferred from Fe and Ni to P in the Fe−P and Ni−P species,[56,75,76] which can be further proved in Fe and Ni XPS spectra (Figure 2b). In the high-resolution Fe 2p spectrum, the binding energy of Fe $2p_{3/2}$ at 707.7 eV

DOI: 10.1021/acsami.7b07142
ACS Appl. Mater. Interfaces 2017, 9, 23852−23858

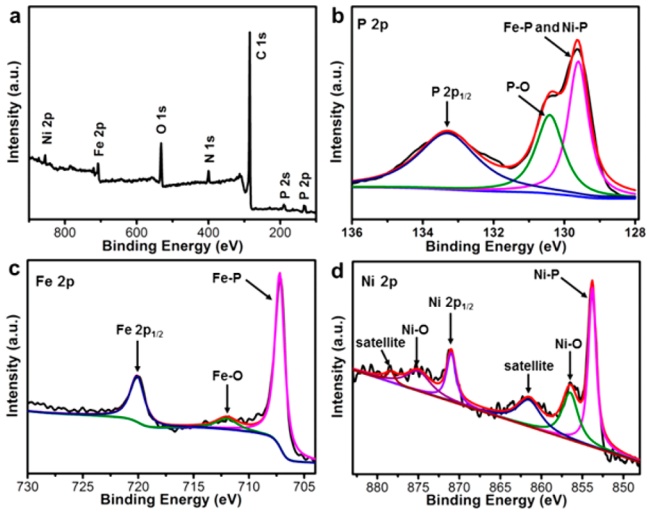

Figure 2. (a) XPS survey spectrum of Fe−Ni−P/rGO-400. High-resolution XPS spectra of (b) P 2p, (c) Fe 2p, and (d) Ni 2p in Fe−Ni−P/rGO-400.

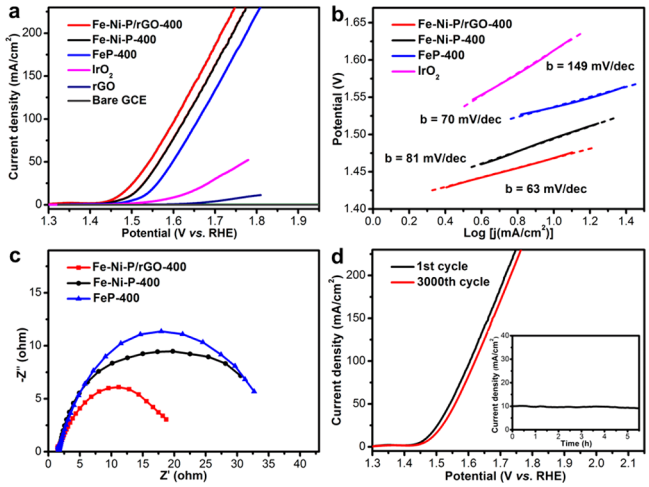

Figure 3. (a) LSV curves, (b) Tafel slopes, and (c) Nyquist plots for Fe−Ni−P/rGO-400, Fe−Ni−P-400, and FeP-400 in 1 M KOH solution. (d) Durability test for the electrochemical OER activity of Fe−Ni−P/rGO-400 (inset: time-dependent current density curve of Fe−Ni−P/rGO-400 under static overpotential of 240 mV) in 1 M KOH solution.

positively shifts from 706.8 eV of elemental Fe, suggesting the formation of Fe−P species. The peak at 712.0 eV corresponding to oxidized iron species stems from the oxidation of the exterior exposed in the air (Figure 2c).[37,42] Six subpeaks can be fitted according to the high-resolution spectrum of Ni 2p (Figure 2d). The Ni 2p bonding energy of 853.4 eV positively shifts from that of elemental Ni at 852.6 eV, supporting the electron transfer from Ni to P and the formation of Ni−P compound.[59] The peaks at 853.4 and 871.7 eV can be assigned to Ni $2p_{3/2}$ and Ni $2p_{1/2}$ of the Ni−P compound. The peaks located at around 856.5 and 875.1 eV can be assigned to Ni $2p_{3/2}$ and Ni $2p_{1/2}$ of the oxidized nickel species, and the satellite peaks for Ni $2p_{3/2}$ and Ni $2p_{1/2}$ are located at 861.7 and 878.0 eV.[32,75,76] All these XPS data clearly demonstrate the successful construction of Fe−Ni−P/rGO-400 via the phosphidation process, in good agreement with powder XRD and HRTEM results above (Figure 2c,d and Figure S7).

Encouraged by the results above, the electrocatalytic OER performance for the Fe−Ni−P/rGO composites has been investigated by rotating disk electrode (RDE) measurements in 1 M KOH solution. From the linear sweep voltammetry (LSV) tests, each sample, including Fe−Ni−O/rGO-400, Fe−Ni−P-400, Fe−Ni−P/rGO-400, and FeP-400 obtained by PCN-600-Fe featuring Fe(III) located in the porphyrin centers, presents characteristic OER catalytic behavior (Figure 3a and Figure S10). It can be seen that Fe−Ni−P-400 shows a better catalytic activity than FeP-400, highlighting the enhancement effect of Ni doping. When the conductive rGO is introduced, the resultant Fe−Ni−P/rGO-400 presents the best OER activity among all catalysts and achieves a current density of 10 mA/cm^2 at an overpotential as low as 240 mV, while the state-of-the-art IrO_2 exhibits a weak overpotential at 400 mV, indicating that Fe−Ni−P/rGO-400 is far superior to the IrO_2 and among the best in all non-noble-metal-based electrocatalysts (Figure 3a and Table S1). Besides, the OER performance of pure rGO and blank glassy carbon electrode (GCE) can be well excluded due to their negligible responses on LSV curves (Figure 3a). The comparison of Fe−Ni−P/rGO-T composites obtained at different oxidation temperatures manifests that Fe−Ni−P/rGO-400, offering both good crystallinity and high graphitized carbon content, exhibits superior activity to others (Figure S11). The better performance of Fe−Ni−P/rGO-400 than Fe−Ni−P-rGO-mix (the physical mixture of PCN-600-Ni and GO) manifests the enhancement effect of strong interaction between Fe−Ni−P and rGO in Fe−Ni−P/rGO-400 (Figure S12). To further explore the influence of Ni contents on OER performance, the PCN-600-$Ni_{0.5}$ precursor has been assembled based on 50% Ni-TCPP and 50% Fe-TCPP linkers. Unfortunately, the resultant Fe−$Ni_{0.5}$-P-400 offers inferior OER activity to Fe−Ni−P-400, indicating that PCN-600-Ni with 100% Ni-TCPP linker is the optimized parameter (Figure S13). Meanwhile, the Tafel slope of Fe−Ni−P/rGO-400 (63 mV/dec) indicates a more favorable kinetics of Fe−Ni−P/rGO-400 than IrO_2 and also presents a fairly good kinetic behavior among all non-noble-metal-based OER electrocatalysts (Figure 3b and Table S1). The OER kinetics of as-synthesized catalysts at the electrode/electrolyte interface can be further evaluated by electrochemical impedance spectroscopy (EIS). The best-performed Fe−Ni−P/rGO-400 catalyst displays a much smaller charge-transfer resistance (R_{ct}) than Fe−Ni−P-400 and FeP-400, suggesting a much faster electron transfer during the electrochemical reaction, ascribed to the improved conductivity via the introduction of GO (Figure 3c). In addition to high activity, excellent stability is also necessary for an ideal OER catalyst. The LSV curve recording 3000 cycles of continuous CV scanning for Fe−Ni−P/rGO-400 shows only a slight difference compared with the initial one, exemplifying its satisfactory stability (Figure 3d). Meanwhile, the chronoamperometry test is also performed to evaluate the stability of electrocatalysts. The current density of Fe−Ni−P/rGO-400 tested at an overpotential of 240 mV for 5 h is pretty stable and remains a very high activity, which indicates the excellent durability of Fe−Ni−P/rGO-400 in the electrochemical process (Figure 3d, inset).

CONCLUSION

In summary, we have rationally fabricated a sheetlike Fe−Ni−P/rGO composite, via a GO-templated MOF growth and following heat treatment and phosphidation process, for efficient OER electrocatalysis by water splitting. By integrating

DOI: 10.1021/acsami.7b07142
ACS Appl. Mater. Interfaces 2017, 9, 23852−23858

the highly porous feature, the synergetic effect between Fe and Ni elements, and the enhanced conductivity of GO, the optimized Fe−Ni−P/rGO-400 composite exhibits superior OER catalytic performance as well as stability in alkaline solution, surpassing the state-of-the-art IrO_2 and being among the most active OER catalysts reported so far. This study offers a novel and rational strategy to the synthesis of high performance electrocatalysts derived from porphyrinic MOF-GO composites with the combination of respective advantages. Considering the universality and modifiability of MOFs, this strategy exhibited here would shed light on the fabrication of advanced nanostructured materials for efficient electrocatalysis.

■ ASSOCIATED CONTENT

Supporting Information

The Supporting Information is available free of charge on the ACS Publications website at DOI: 10.1021/acsami.7b07142.

SEM image, powder XRD patterns, N_2 sorption isotherms, electrochemical activity; Table S1 (PDF)

■ AUTHOR INFORMATION

Corresponding Author

*E-mail: jianglab@ustc.edu.cn.

ORCID

Hai-Long Jiang: 0000-0002-2975-7977

Author Contributions

X.F. and L.J. contributed equally.

Notes

The authors declare no competing financial interest.

■ ACKNOWLEDGMENTS

This work is supported by the NSFC (21371162, 21673213, and 21521001), the National Research Fund for Fundamental Key Project (2014CB931803), and the Recruitment Program of Global Youth Experts and Key Laboratory of Functional Inorganic Material Chemistry (Heilongjiang University), Ministry of Education.

■ REFERENCES

(1) Hunter, B. M.; Gray, H. B.; Müller, A. M. Earth-Abundant Heterogeneous Water Oxidation Catalysts. *Chem. Rev.* **2016**, *116*, 14120−14136.

(2) Zou, X.; Zhang, Y. Noble Metal-Free Hydrogen Evolution Catalysts for Water Splitting. *Chem. Soc. Rev.* **2015**, *44*, 5148−5180.

(3) Suen, N.-T.; Hung, S.-F.; Quan, Q.; Zhang, N.; Xu, Y.-J.; Chen, H. M. Electrocatalysis for the Oxygen Evolution Reaction: Recent Development and Future Perspectives. *Chem. Soc. Rev.* **2017**, *46*, 337−365.

(4) Chen, D.; Chen, C.; Baiyee, Z. M.; Shao, Z.; Ciucci, F. Nonstoichiometric Oxides as Low-Cost and Highly-Efficient Oxygen Reduction/Evolution Catalysts for Low-Temperature Electrochemical Devices. *Chem. Rev.* **2015**, *115*, 9869−9921.

(5) Zhu, Y. P.; Guo, C.; Zheng, Y.; Qiao, S.-Z. Surface and Interface Engineering of Noble-Metal-Free Electrocatalysts for Efficient Energy Conversion Processes. *Acc. Chem. Res.* **2017**, *50*, 915−923.

(6) Xu, Y.; Kraft, M.; Xu, R. Metal-Free Carbonaceous Electrocatalysts and Photocatalysts for Water Splitting. *Chem. Soc. Rev.* **2016**, *45*, 3039−3052.

(7) Morales-Guio, C. G.; Stern, L.-A.; Hu, X. Nanostructured Hydrotreating Catalysts for Electrochemical Hydrogen Evolution. *Chem. Soc. Rev.* **2014**, *43*, 6555−6569.

(8) Zhang, W.; Lai, W.; Cao, R. Energy-Related Small Molecule Activation Reactions: Oxygen Reduction and Hydrogen and Oxygen Evolution Reactions Catalyzed by Porphyrin- and Corrole-Based Systems. *Chem. Rev.* **2017**, *117*, 3717−3797.

(9) Gong, M.; Zhou, W.; Tsai, M.-C.; Zhou, J.; Guan, M.; Lin, M. C.; Zhang, B.; Hu, Y.; Wang, D.-Y.; Yang, J.; Pennycook, S. J.; Hwang, B.-J.; Dai, H. Nanoscale Nickel Oxide/Nickel Heterostructures for Active Hydrogen Evolution Electrocatalysis. *Nat. Commun.* **2014**, *5*, 4695.

(10) Zheng, Y.; Jiao, Y.; Zhu, Y.; Cai, Q.; Vasileff, A.; Li, L. H.; Han, Y.; Chen, Y.; Qiao, S.-Z. Molecule-Level g-C_3N_4 Coordinated Transition Metals as a New Class of Electrocatalysts for Oxygen Electrode Reactions. *J. Am. Chem. Soc.* **2017**, *139*, 3336−3339.

(11) Zhao, S.; Wang, Y.; Dong, J.; He, C.-T.; Yin, H.; An, P.; Zhao, K.; Zhang, X.; Gao, C.; Zhang, L.; Lv, J.; Wang, J.; Zhang, J.; Khattak, A. M.; Khan, N. A.; Wei, Z.; Zhang, J.; Liu, S.; Zhao, H.; Tang, Z. Ultrathin Metal-Organic Framework Nanosheets for Electrocatalytic Oxygen Evolution. *Nat. Energy* **2016**, *1*, 16184.

(12) Wang, J.; Li, K.; Zhong, H.-X.; Xu, D.; Wang, Z.-L.; Jiang, Z.; Wu, Z.-J.; Zhang, X.-B. Synergistic Effect between Metal-Nitrogen-Carbon Sheets and NiO Nanoparticles for Enhanced Electrochemical Water-Oxidation Performance. *Angew. Chem., Int. Ed.* **2015**, *54*, 10530−10534.

(13) Guo, C.; Zheng, Y.; Ran, J.; Xie, F.; Jaroniec, M.; Qiao, S.-Z. Engineering High-Energy Interfacial Structures for High-Performance Oxygen-Involving Electrocatalysis. *Angew. Chem., Int. Ed.* **2017**, *56*, 8539−8543.

(14) Zhou, W.; Wu, X.-J.; Cao, X.; Huang, X.; Tan, C.; Tian, J.; Liu, H.; Wang, J.; Zhang, H. Ni_3S_2 Nanorods/Ni Foam Composite Electrode with Low Overpotential for Electrocatalytic Oxygen Evolution. *Energy Environ. Sci.* **2013**, *6*, 2921−2924.

(15) Suntivich, J.; May, K. J.; Gasteiger, H. A.; Goodenough, J. B.; Shao-Horn, Y. A Perovskite Oxide Optimized for Oxygen Evolution Catalysis from Molecular Orbital Principles. *Science* **2011**, *334*, 1383−1385.

(16) Bediako, D. K.; Lassalle-Kaiser, B.; Surendranath, Y.; Yano, J.; Yachandra, V. K.; Nocera, D. G. Structure-Activity Correlations in a Nickel-Borate Oxygen Evolution Catalyst. *J. Am. Chem. Soc.* **2012**, *134*, 6801−6809.

(17) Fang, Y.-H.; Liu, Z.-P. Mechanism and Tafel Lines of Electro-Oxidation of Water to Oxygen on RuO_2(110). *J. Am. Chem. Soc.* **2010**, *132*, 18214−18222.

(18) Bayatsarmadi, B.; Zheng, Y.; Tang, Y.; Jaroniec, M.; Qiao, S.-Z. Significant Enhancement of Water Splitting Activity of N-Carbon Electrocatalyst by Trace Level Co Doping. *Small* **2016**, *12*, 3703−3711.

(19) Li, F.; Zhang, B.; Li, X.; Jiang, Y.; Chen, L.; Li, Y.; Sun, L. Highly Efficient Oxidation of Water by a Molecular Catalyst Immobilized on Carbon Nanotubes. *Angew. Chem., Int. Ed.* **2011**, *50*, 12276−12279.

(20) Zhao, Y.; Jia, X.; Chen, G.; Shang, L.; Waterhouse, G. I. N.; Wu, L.-Z.; Tung, C.-H.; O'Hare, D.; Zhang, T. Ultrafine NiO Nanosheets Stabilized by TiO_2 from Monolayer NiTi-LDH Precursors: An Active Water Oxidation Electrocatalyst. *J. Am. Chem. Soc.* **2016**, *138*, 6517−6524.

(21) Ling, T.; Yan, D. Y.; Jiao, Y.; Wang, H.; Zheng, Y.; Zheng, X.; Mao, J.; Du, X.-W.; Hu, Z.; Jaroniec, M.; Qiao, S.-Z. Engineering Surface Atomic Structure of Single-Crystal Cobalt (II) Oxide Nanorods for Superior Electrocatalysis. *Nat. Commun.* **2016**, *7*, 12876.

(22) Subbaraman, R.; Tripkovic, D.; Chang, K.-C.; Strmcnik, D.; Paulikas, A. P.; Hirunsit, P.; Chan, M.; Greeley, J.; Stamenkovic, V.; Markovic, N. M. Trends in Activity for the Water Electrolyser Reactions on 3*d* M(Ni,Co,Fe,Mn) Hydr(oxy)oxide Catalysts. *Nat. Mater.* **2012**, *11*, 550−557.

(23) Lu, Z.; Wang, H.; Kong, D.; Yan, K.; Hsu, P.-C.; Zheng, G.; Yao, H.; Liang, Z.; Sun, X.; Cui, Y. Electrochemical Tuning of Layered Lithium Transition Metal Oxides for Improvement of Oxygen Evolution Reaction. *Nat. Commun.* **2014**, *5*, 4345.

(24) Liang, H.; Meng, F.; Cabán-Acevedo, M.; Li, L.; Forticaux, A.; Xiu, L.; Wang, Z.; Jin, S. Hydrothermal Continuous Flow Synthesis and Exfoliation of NiCo Layered Double Hydroxide Nanosheets for Enhanced Oxygen Evolution Catalysis. *Nano Lett.* **2015**, *15*, 1421−1427.

DOI: 10.1021/acsami.7b07142
ACS Appl. Mater. Interfaces 2017, 9, 23852−23858

(25) Zhu, Y. P.; Ma, T. Y.; Jaroniec, M.; Qiao, S.-Z. Self-Templating Synthesis of Hollow Co_3O_4 Microtube Arrays for Highly Efficient Water Electrolysis. *Angew. Chem., Int. Ed.* **2017**, *56*, 1324−1328.
(26) Jin, H.; Wang, J.; Su, D.; Wei, Z.; Pang, Z.; Wang, Y. In situ Cobalt-Cobalt Oxide/N-Doped Carbon Hybrids as Superior Bifunctional Electrocatalysts for Hydrogen and Oxygen Evolution. *J. Am. Chem. Soc.* **2015**, *137*, 2688−2694.
(27) Xu, L.; Jiang, Q.; Xiao, Z.; Li, X.; Huo, J.; Wang, S.; Dai, L. Plasma-Engraved Co_3O_4 Nanosheets with Oxygen Vacancies and High Surface Area for the Oxygen Evolution Reaction. *Angew. Chem., Int. Ed.* **2016**, *55*, 5277−5281.
(28) Burke, M. S.; Kast, M. G.; Trotochaud, L.; Smith, A. M.; Boettcher, S. W. Cobalt-Iron (Oxy)hydroxide Oxygen Evolution Electrocatalysts: The Role of Structure and Composition on Activity, Stability, and Mechanism. *J. Am. Chem. Soc.* **2015**, *137*, 3638−3648.
(29) Li, Z.; Shao, M.; An, H.; Wang, Z.; Xu, S.; Wei, M.; Evans, D. G.; Duan, X. Fast Electrosynthesis of Fe-Containing Layered Double Hydroxide Arrays Toward Highly Efficient Electrocatalytic Oxidation Reactions. *Chem. Sci.* **2015**, *6*, 6624−6631.
(30) Surendranath, Y.; Lutterman, D. A.; Liu, Y.; Nocera, D. G. Nucleation, Growth, and Repair of a Cobalt-Based Oxygen Evolving Catalyst. *J. Am. Chem. Soc.* **2012**, *134*, 6326−6336.
(31) Shi, Y.; Zhang, B. Recent Advances in Transition Metal Phosphide Nanomaterials: Synthesis and Applications in Hydrogen Evolution Reaction. *Chem. Soc. Rev.* **2016**, *45*, 1529−1541.
(32) Zhuo, J.; Cabán-Acevedo, M.; Liang, H.; Samad, L.; Ding, Q.; Fu, Y.; Li, M.; Jin, S. High-Performance Electrocatalysis for Hydrogen Evolution Reaction Using Se-Doped Pyrite-Phase Nickel Diphosphide Nanostructures. *ACS Catal.* **2015**, *5*, 6355−6361.
(33) Stern, L.-A.; Feng, L.; Song, F.; Hu, X. Ni_2P as a Janus Catalyst for Water Splitting: The Oxygen Evolution Activity of Ni_2P Nanoparticles. *Energy Environ. Sci.* **2015**, *8*, 2347−2351.
(34) Xiao, P.; Chen, W.; Wang, X. A Review of Phosphide-Based Materials for Electrocatalytic Hydrogen Evolution. *Adv. Energy Mater.* **2015**, *5*, 1500985.
(35) Dutta, A.; Pradhan, N. Developments of Metal Phosphides as Efficient OER Precatalysts. *J. Phys. Chem. Lett.* **2017**, *8*, 144−152.
(36) Sun, M.; Liu, H.; Qu, J.; Li, J. Earth-Rich Transition Metal Phosphide for Energy Conversion and Storage. *Adv. Energy Mater.* **2016**, *6*, 1600087.
(37) Anantharaj, S.; Ede, S. R.; Sakthikumar, K.; Karthick, K.; Mishra, S.; Kundu, S. Recent Trends and Perspectives in Electrochemical Water Splitting with an Emphasis on Sulfide, Selenide, and Phosphide Catalysts of Fe, Co, and Ni: A Review. *ACS Catal.* **2016**, *6*, 8069−8097.
(38) Wang, X.; Yang, J.; Yin, H.; Song, R.; Tang, Z. "Raisin Bun"-Like Nanocomposites of Palladium Clusters and Porphyrin for Superior Formic Acid Oxidation. *Adv. Mater.* **2013**, *25*, 2728−2732.
(39) Fu, S.; Zhu, C.; Song, J.; Engelhard, M. H.; Li, X.; Du, D.; Lin, Y. Highly Ordered Mesoporous Bimetallic Phosphides as Efficient Oxygen Evolution Electrocatalysts. *ACS Energy Lett.* **2016**, *1*, 792−796.
(40) Mendoza-Garcia, A.; Zhu, H.; Yu, Y.; Li, Q.; Zhou, L.; Su, D.; Kramer, M. J.; Sun, S. Controlled Anisotropic Growth of Co-Fe-P from Co-Fe-O Nanoparticles. *Angew. Chem., Int. Ed.* **2015**, *54*, 9642−9645.
(41) Li, D.; Baydoun, H.; Verani, C. N.; Brock, S. L. Efficient Water Oxidation Using CoMnP Nanoparticles. *J. Am. Chem. Soc.* **2016**, *138*, 4006−4009.
(42) Tang, C.; Zhang, R.; Lu, W.; He, L.; Jiang, X.; Asiri, A. M.; Sun, X. Fe-Doped CoP Nanoarray: A Monolithic Multifunctional Catalyst for Highly Efficient Hydrogen Generation. *Adv. Mater.* **2017**, *29*, 1602441.
(43) He, P.; Yu, X.-Y.; Lou, X. W. Carbon-Incorporated Nickel-Cobalt Mixed Metal Phosphide Nanoboxes with Enhanced Electrocatalytic Activity for Oxygen Evolution. *Angew. Chem., Int. Ed.* **2017**, *56*, 3897−3900.
(44) Sun, J.; Yin, H.; Liu, P.; Wang, Y.; Yao, X.; Tang, Z.; Zhao, H. Molecular Engineering of Ni-/Co-Porphyrin Multilayers on Reduced Graphene Oxide Sheets as Bifunctional Catalysts for Oxygen Evolution and Oxygen Reduction Reactions. *Chem. Sci.* **2016**, *7*, 5640−5646.
(45) Duan, J.; Chen, S.; Vasileff, A.; Qiao, S.-Z. Anion and Cation Modulation in Metal Compounds for Bifunctional Overall Water Splitting. *ACS Nano* **2016**, *10*, 8738−8745.
(46) Wang, X.; Li, W.; Xiong, D.; Petrovykh, D. Y.; Liu, L. Bifunctional Nickel Phosphide Nanocatalysts Supported on Carbon Fiber Paper for Highly Efficient and Stable Overall Water Splitting. *Adv. Funct. Mater.* **2016**, *26*, 4067−4077.
(47) Zhu, Y.-P.; Liu, Y.-P.; Ren, T.-Z.; Yuan, Z.-Y. Self-Supported Cobalt Phosphide Mesoporous Nanorod Arrays: A Flexible and Bifunctional Electrode for Highly Active Electrocatalytic Water Reduction and Oxidation. *Adv. Funct. Mater.* **2015**, *25*, 7337−7347.
(48) Zhang, G.; Wang, G.; Liu, Y.; Liu, H.; Qu, J.; Li, J. Highly Active and Stable Catalysts of Phytic Acid-Derivative Transition Metal Phosphides for Full Water Splitting. *J. Am. Chem. Soc.* **2016**, *138*, 14686−14693.
(49) Tian, J.; Liu, Q.; Asiri, A. M.; Sun, X. Self-Supported Nanoporous Cobalt Phosphide Nanowire Arrays: An Efficient 3D Hydrogen-Evolving Cathode over the Wide Range of pH 0−14. *J. Am. Chem. Soc.* **2014**, *136*, 7587−7590.
(50) Tang, H.; Yin, H.; Wang, J.; Yang, N.; Wang, D.; Tang, Z. Molecular Architecture of Cobalt Porphyrin Multilayers on Reduced Graphene Oxide Sheets for High-Performance Oxygen Reduction Reaction. *Angew. Chem., Int. Ed.* **2013**, *52*, 5585−5590.
(51) Zhou, H.-C.; Long, J. R.; Yaghi, O. M. Introduction to Metal-Organic Frameworks. *Chem. Rev.* **2012**, *112*, 673−674.
(52) Zhou, H.-C.; Kitagawa, S. Metal-Organic Frameworks (MOFs). *Chem. Soc. Rev.* **2014**, *43*, 5415−5418.
(53) Zhu, Q.-L.; Xu, Q. Metal-Organic Framework Composite. *Chem. Soc. Rev.* **2014**, *43*, 5468−5512.
(54) Li, B.; Wen, H.-M.; Cui, Y.; Zhou, W.; Qian, G.; Chen, B. Emerging Multifunctional Metal-Organic Framework Materials. *Adv. Mater.* **2016**, *28*, 8819−8860.
(55) He, L.; Liu, Y.; Liu, J.; Xiong, Y.; Zheng, J.; Liu, Y.; Tang, Z. Core-Shell Noble-Metal@Metal-Organic-Framework Nanoparticles with Highly Selective Sensing Property. *Angew. Chem., Int. Ed.* **2013**, *52*, 3741−3745.
(56) Jiang, H.-L.; Liu, B.; Lan, Y.-Q.; Kuratani, K.; Akita, T.; Shioyama, H.; Zong, F.; Xu, Q. From Metal-Organic Framework to Nanoporous Carbon: Toward a Very High Surface Area and Hydrogen Uptake. *J. Am. Chem. Soc.* **2011**, *133*, 11854−11857.
(57) Zhao, D.; Shui, J.-L.; Chen, C.; Chen, X.; Reprogle, B. M.; Wang, D.; Liu, D.-J. Iron Imidazolate Framework as Precursor for Electrocatalysts in Polymer Electrolyte Membrane Fuel Cells. *Chem. Sci.* **2012**, *3*, 3200−3205.
(58) Kaneti, Y. V.; Tang, J.; Salunkhe, R. R.; Jiang, X.; Yu, A.; Wu, K. C.-W.; Yamauchi, Y. Nanoarchitectured Design of Porous Materials and Nanocomposites from Metal-Organic Frameworks. *Adv. Mater.* **2017**, *29*, 1604898.
(59) Hou, Y.; Huang, T.; Wen, Z.; Mao, S.; Cui, S.; Chen, J. Metal-Organic Framework-Derived Nitrogen-Doped Core-Shell-Structured Porous Fe/Fe_3C@C Nanoboxes Supported on Graphene Sheets for Efficient Oxygen Reduction Reactions. *Adv. Energy Mater.* **2014**, *4*, 1400337.
(60) Shen, K.; Chen, X.; Chen, J.; Li, Y. Development of MOF-Derived Carbon-Based Nanomaterials for Efficient Catalysis. *ACS Catal.* **2016**, *6*, 5887−5903.
(61) Ma, S.; Goenaga, G. A.; Call, A. V.; Liu, D.-J. Cobalt Imidazolate Framework as Precursor for Oxygen Reduction Reaction Electrocatalysts. *Chem. - Eur. J.* **2011**, *17*, 2063−2067.
(62) Lin, Q.; Bu, X.; Kong, A.; Mao, C.; Zhao, X.; Bu, F.; Feng, P. New Heterometallic Zirconium Metalloporphyrin Frameworks and Their Heteroatom-Activated High-Surface-Area Carbon Derivatives. *J. Am. Chem. Soc.* **2015**, *137*, 2235−2238.
(63) Zhao, S.; Yin, H.; Du, L.; He, L.; Zhao, K.; Chang, L.; Yin, G.; Zhao, H.; Liu, S.; Tang, Z. Carbonized Nanoscale Metal-Organic

DOI: 10.1021/acsami.7b07142
ACS Appl. Mater. Interfaces 2017, 9, 23852−23858

Frameworks as High Performance Electrocatalyst for Oxygen Reduction Reaction. *ACS Nano* **2014**, *8*, 12660−12668.
(64) Liu, J.; Zhu, D.; Guo, C.; Vasileff, A.; Qiao, S.-Z. Design Strategies toward Advanced MOF-Derived Electrocatalysts for Energy-Conversion Reactions. *Adv. Energy Mater.* **2017**, 1700518.
(65) Jiao, L.; Zhou, Y.-X.; Jiang, H.-L. Metal-Organic Framework-Based CoP/Reduced Graphene Oxide: High-Performance Bifunctional Electrocatalyst for Overall Water Splitting. *Chem. Sci.* **2016**, *7*, 1690−1695.
(66) You, B.; Jiang, N.; Sheng, M.; Gul, S.; Yano, J.; Sun, Y. High-Performance Overall Water Splitting Electrocatalysts Derived From Cobalt-Based Metal-Organic Frameworks. *Chem. Mater.* **2015**, *27*, 7636−7642.
(67) Song, J.; Zhu, C.; Xu, B. Z.; Fu, S.; Engelhard, M. H.; Ye, R.; Du, D.; Beckman, S. P.; Lin, Y. Bimetallic Cobalt-Based Phosphide Zeolitic Imidazolate Framework: CoP_x Phase-Dependent Electrical Conductivity and Hydrogen Atom Adsorption Energy for Efficient Overall Water Splitting. *Adv. Energy Mater.* **2017**, *7*, 1601555.
(68) Yu, X.-Y.; Feng, Y.; Guan, B.; Lou, X. W.; Paik, U. Carbon Coated Porous Nickel Phosphides Nanoplates for Highly Efficient Oxygen Evolution Reaction. *Energy Environ. Sci.* **2016**, *9*, 1246−1250.
(69) Zhang, T.; Du, J.; Xi, P.; Xu, C. Hybrids of Cobalt/Iron Phosphides Derived from Bimetal- Organic Frameworks as Highly Efficient Electrocatalysts for Oxygen Evolution Reaction. *ACS Appl. Mater. Interfaces* **2017**, *9*, 362−370.
(70) Ma, T. Y.; Dai, S.; Jaroniec, M.; Qiao, S.-Z. Metal-Organic Framework Derived Hybrid Co_3O_4-Carbon Porous Nanowire Arrays as Reversible Oxygen Evolution Electrodes. *J. Am. Chem. Soc.* **2014**, *136*, 13925−13931.
(71) Wang, K.; Feng, D.; Liu, T.-F.; Su, J.; Yuan, S.; Chen, Y.-P.; Bosch, M.; Zou, X.; Zhou, H.-C. A Series of Highly Stable Mesoporous Metalloporphyrin Fe-MOFs. *J. Am. Chem. Soc.* **2014**, *136*, 13983−13986.
(72) Chen, S.; Duan, J.; Jaroniec, M.; Qiao, S.-Z. Nitrogen and Oxygen Dual-Doped Carbon Hydrogel Film as a Substrate-Free Electrode for Highly Efficient Oxygen Evolution Reaction. *Adv. Mater.* **2014**, *26*, 2925−2930.
(73) Tian, J.; Liu, Q.; Asiri, A. M.; Alamry, K. A.; Sun, X. Ultrathin Graphitic C_3N_4 Nanosheets/Graphene Composites: Efficient Organic Electrocatalyst for Oxygen Evolution Reaction. *ChemSusChem* **2014**, *7*, 2125−2130.
(74) Zhao, Y.; Nakamura, R.; Kamiya, K.; Nakanishi, S.; Hashimoto, K. Nitrogen-Doped Carbon Nanomaterials as Non-Metal Electrocatalysts for Water Oxidation. *Nat. Commun.* **2013**, *4*, 2390.
(75) Jiang, P.; Liu, Q.; Liang, Y.; Tian, J.; Asiri, A. M.; Sun, X. A Cost-Effective 3D Hydrogen Evolution Cathode with High Catalytic Activity: FeP Nanowire Array as the Active Phase. *Angew. Chem., Int. Ed.* **2014**, *53*, 12855−12859.
(76) Grosvenor, A. P.; Wik, S. D.; Cavell, R. G.; Mar, A. Examination of the Bonding in Binary Transition-Metal Monophosphides MP (M = Cr, Mn, Fe, Co) by X-Ray Photoelectron Spectroscopy. *Inorg. Chem.* **2005**, *44*, 8988−8998.

DOI: 10.1021/acsami.7b07142
ACS Appl. Mater. Interfaces 2017, 9, 23852−23858